RSC Advances

PAPER

View Article Online
View Journal | View Issue

Check for updates

Cite this: *RSC Adv.*, 2024, **14**, 677

# *Vitex Negundo*–$Fe_3O_4$–CuO green nanocatalyst (*VN*–$Fe_3O_4$–CuO): synthesis of pyrazolo[3,4-*c*] pyrazole derivatives *via* the cyclization of isoniazid with pyrazole and their antimicrobial activity, cytotoxicity, and molecular docking studies†

Idhayadhulla Akbar, *[a] Janani Mullaivendhan,[a] Anis Ahamed[b] and Hossam M. Aljawdah[c]

In this study, we developed a novel pyrazolo[3,4-*c*]pyrazole derivative with antibacterial and antifungal activities that shows great potential for treating infectious diseases. To evaluate the binding affinity of 1AJ0 and 1AI9 proteins for developing potent antibacterial and antifungal compounds, we used the *Vitex negundo* (*VN*) leaf extract as the capping and reducing agent and reacted it with $Fe_2O_3$ and $Cu(OAc)_2$ solutions to synthesize the *VN*–$Fe_3O_4$–CuO nanocatalyst. The newly synthesized compounds were confirmed using Fourier transform infrared spectroscopy, transmission electron microscopy, UV-visible spectroscopy, and X-ray diffraction analyses. Antibacterial screening revealed that compound **1g** was highly active against *Escherichia coli* (MIC: 1 μg $mL^{-1}$) and was much more effective than the standard ciprofloxacin. Compound **1b** showed a higher antifungal activity than clotrimazole against *Candida albicans* (MIC: 0.25 μg $mL^{-1}$) and cytotoxic activity against MCF-7 cancer cell lines. Compounds **1a–1l** were exhibited low cytotoxicity activity compared to the standard doxorubicin ($LC_{50}$: 21.05 ± 0.82 μg $mL^{-1}$). To further support the discovery of new active antibacterial agents, compounds **1g** and **1b** and proteins 1AJ0 and 1AI9 were examined using the AutoDock Vina program and were compared with the standards ciprofloxacin and clotrimazole. With the 1AJ0 protein, compound **1g** had a higher docking score (−3.7 kcal $mol^{-1}$) than ciprofloxacin (−5.6 kcal $mol^{-1}$), and with the 1AI9 protein, compound **1b** had a higher docking score (−4.8 kcal $mol^{-1}$) than clotrimazole (−4.4 kcal $mol^{-1}$). Additionally, molecular dynamics simulation was used to investigate the most probable binding mode of compounds **1b** and **1g** with 1AI9 and 1AJ0, respectively. The *VN*–$Fe_3O_4$–CuO catalyst was used to prepare pyrazolo[3,4-*c*] pyrazole derivatives, which were successfully characterized and screened for antimicrobial and cytotoxic activities, molecular docking, and molecular dynamics simulation studies.

Received 5th October 2023
Accepted 5th December 2023

DOI: 10.1039/d3ra06771h

rsc.li/rsc-advances

Open Access Article. Published on 02 de gener 2024. Downloaded on 16/2/2026 20:04:58.
This article is licensed under a Creative Commons Attribution-NonCommercial 3.0 Unported Licence.

## 1. Introduction

Pyrazolo[4,3-*c*]pyrazoles derivatives are an intriguing class of compounds that act as isosteric purine derivatives with potential pharmacological effects. They are also useful intermediates and end products in the synthesis of physiologically and pharmacologically active compounds, such as dyes and antibiotics, that contain pyrazoles.[1–3] The ATP (adenosine triphosphate)-binding site of protein kinases is the target for a family of substances known as tetrahydropyrrolo[3,4-*c*]pyrazoles.[4] Pyrazoles derivatives contain N–N bonds and are found in five-membered heterocycles,[5] and are commonly applied in biochemical and pharmaceutical fields (Fig. 1).[6]

Monocyclic pyrazoles can serve as synthetic scaffolds for fused heterocyclic systems, including pyrazolo-fused pyrimidines, quinolones, pyridines, thiazoles, isoquinolines, imidazoles, diazepines, and triazines.[7] They have potent biological activities, including immunostimulatory, anticancer, antioxidant, antibacterial, and antiviral effects.[8]

Some bicyclic heterocycles are effective hGSK-3a inhibitors and can treat esophageal and gastrointestinal mucosal injuries.[9] Pyrazolo[3,4-*c*]pyrazoles derivatives are used to treat autoimmune and inflammatory diseases because of their diverse

[a]*Research Department of Chemistry, Nehru Memorial College (Affiliated Bharathidasan University), Puthanampatti, 621007, Tamil Nadu, India. E-mail: a.idhayadhulla@gmail.com*

[b]*Department of Botany and Microbiology, College of Science, King Saud University, P. O. Box 2455, Riyadh 11451, Saudi Arabia*

[c]*Department of Zoology, College of Science, King Saud University, P. O. Box 2455, Riyadh 11451, Saudi Arabia*

† Electronic supplementary information (ESI) available: The experimental procedures for the cytotoxic activity of compounds (**1a–1l**), molecular dynamics simulation studies, and NMR studies. See DOI: https://doi.org/10.1039/d3ra06771h

© 2024 The Author(s). Published by the Royal Society of Chemistry

Open Access Article. Published on 02 de gener 2024. Downloaded on 16/2/2026 20:04:58.
This article is licensed under a Creative Commons Attribution-NonCommercial 3.0 Unported Licence.

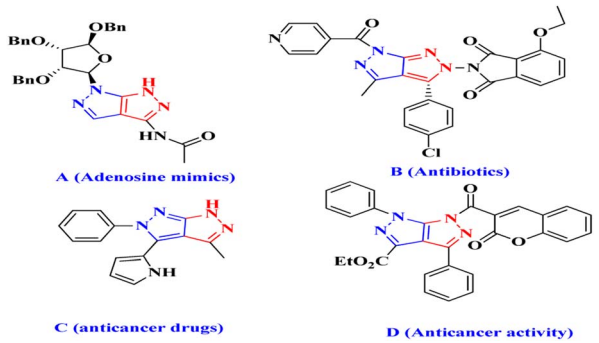


Fig. 1 Bioactive pyrazolo[3,4-*c*]pyrazoles derivatives.

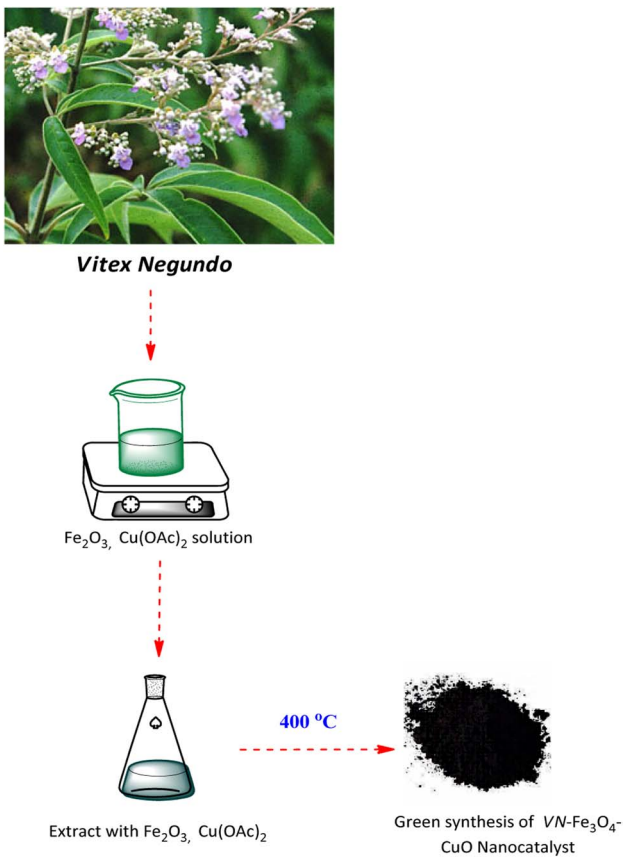


Scheme 1 Synthesis of the *VN*–$Fe_3O_4$–CuO nanocatalyst.

pharmacological and biological properties. Adenosine mimics,[10] antibiotics,[11] and anticancer drugs[12] are examples of compounds that inhibit liver cancer growth in HepG2 cells (anticancer activity) (D)[13] (Fig. 1). Additionally, various medications have been shown to contain pyrazolo[3,4-*c*]pyrazole derivatives, which is a physiologically active molecule.[14] Previously documented techniques include the reaction of 4-arylidenepyrazol-5-ones with hydrazine and hydrazide to produce physiologically active substituted pyrazolo[3,4-*c*] pyrazoles derivatives.[15] Nanotechnology involves applying structures at the nanoscale (1–100 nm) by controlling their size and shape, specifically using nanocatalysts.[16] The

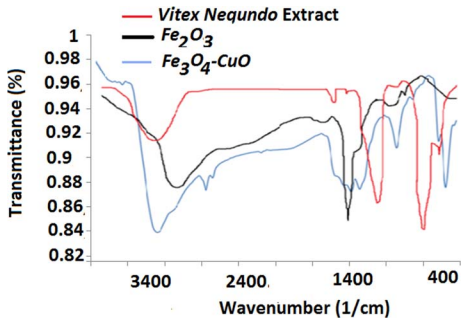


Fig. 2 FTIR spectrum of the *VN*–$Fe_3O_4$–CuO nanocatalyst.

synthesis of nanomaterials using plant extracts, specifically including Ag,[17] Au,[18] Cu,[19] Pd,[20] CuO,[21] MgO,[22] ZnO,[23] and Cu catalysts[24] is an example of green synthesis. Metal nanocatalysts are inexpensive, environment-friendly, size-dependent, and exhibit desirable electrical properties.[25] *Vitex Negundo* (*VN*) is an effective plant used in South Asia, China, East Africa, Japan, Indonesia, and South America.[26] It belongs to the Verbenaceae family and comprises 250 species. *VN* contains anticancer, antifungal, antibacterial, and anti-inflammatory compounds.[27] There is a high demand for nanocatalysts due to their adaptability and outstanding biological, catalytic, and atomic activities.[28] This study focused on analysing the *VN*–$Fe_3O_4$–CuO nanocatalyst because it represents the first comprehensive investigation of the use of *VN* powder extract *VN*–$Fe_3O_4$–CuO nanocatalyst for the synthesis of pyrazolo[3,4-*c*] pyrazole derivatives, which exhibited potent antimicrobial and cytotoxic activities. Molecular docking and molecular dynamics simulations were performed to further investigate the underlying mechanisms of these activities.

## 2. Materials and methods

### 2.1. Reagents and materials

$^1$H and $^{13}$C NMR analyses were carried out using Bruker DRX-300 MHz and 75 MHz spectrometers. FT-IR (KBr) spectra, ranging from 4000–400 $cm^{-1}$, were obtained on a Nicolet iS5 instrument from Thermo Scientific. The silica gel plates were purified using thin-layer chromatography. A Varioel III elemental analyser was used to calculate the percentages (%) of C, H, S, and N. Mass spectra were recorded on a Clarus 690 – SQ8MS (EI) instrument from PerkinElmer GCMS.

### 2.2. Preparation of the *Vitex Negundo* powder

Crushed *Vitex Negundo* leaves were sieved through 20# mesh after being crushed into a fine powder. To prepare the leaf extract, 200 mL of double-distilled water was boiled with 5 g of powdered leaves for 10 min. The filtered broth was stored at 41 °C after it had been filtered through a 0.2 mm filter for a week. The synthesis of *VN*–$Fe_3O_4$–CuO nanocatalyst is outlined in Scheme 1.

### 2.3. The synthesis of *VN*–$Fe_3O_4$–CuO nanocatalyst

The *VN* powder extract (50 mL) was added to a mixed aqueous solution containing 1.0 mmol $Cu(OAc)_2$, and 1.0 mmol iron(III)


© 2024 The Author(s). Published by the Royal Society of Chemistry

Open Access Article. Published on 02 de gener 2024. Downloaded on 16/2/2026 20:04:58.
This article is licensed under a Creative Commons Attribution-NonCommercial 3.0 Unported Licence.

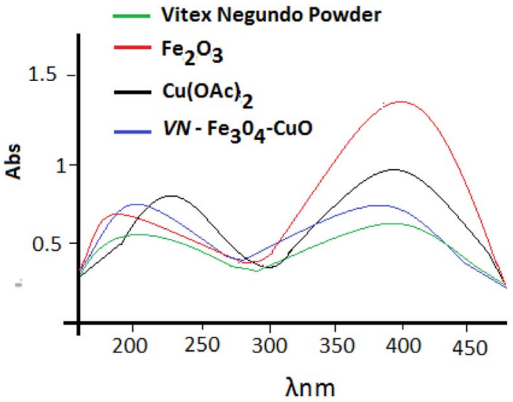


Fig. 3 UV-vis spectra of the *VN*–$Fe_3O_4$–CuO nanocatalyst.

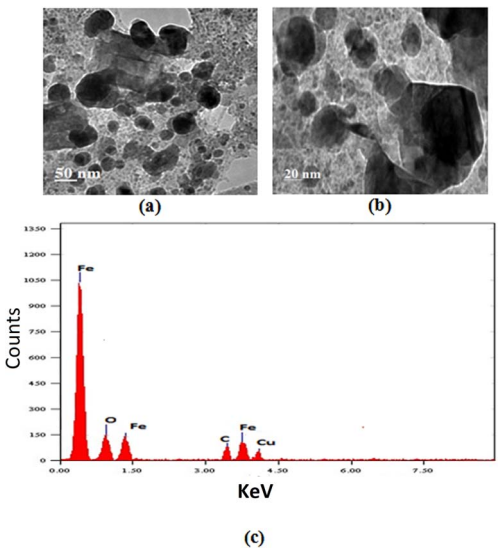


Fig. 4 TEM image for *VN*–$Fe_3O_4$–CuO nanocatalyst: (a) 50 nm and (b) 20 nm, and (c) an EDAX of the *VN*–$Fe_3O_4$–CuO nanocatalyst.

oxide. Following the addition of the plant extract, bioreduction occurred, resulting in the formation of the $Fe_3O_4$. The *VN*–$Fe_3O_4$–CuO nanocatalyst was purified by centrifugation at 10 000 rpm for 20 min. The mixture was refluxed for 1 h, during which the solution's original colour changed to dark brown, indicating the formation of the *VN*–$Fe_3O_4$–Cu nanocatalyst. The resulting nanocatalyst was then dried at 40 °C and then converted into the *VN*–$Fe_3O_4$–CuO nanocatalyst.

### 2.4. Characterization of the synthesized *VN*–$Fe_3O_4$–CuO nanocatalyst and pyrazolo[3,4-*c*]pyrazole derivatives

A spectrophotometer was used to monitor the bioreduction of iron salt, and a quartz cuvette was used as the standard. The UV-vis spectrum of *VN*–$Fe_3O_4$–CuO nanocatalyst was recorded in the range of 200 to 600 nm. We used a Nicolect iS5 FTIR spectrometer (4000–400 $cm^{-1}$) obtained from Thermo Scientific to record the IR spectra of the *VN* powder extract, $Fe_3O_4$, and *VN*–$Fe_3O_4$–CuO nanocatalyst. The *VN*–$Fe_3O_4$–CuO nanocatalyst was examined

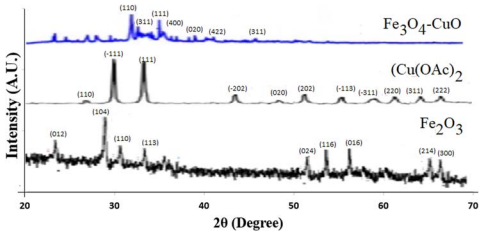


Fig. 5 XRD patterns of the *VN*–$Fe_3O_4$–CuO nanocatalyst.

using TEM (JEOL, JAM-1011) to obtain a *VN*–$Fe_3O_4$–CuO nanocatalyst of approximate size of 50 nm. The *VN*–$Fe_3O_4$–CuO nanocatalyst was poured onto the grids made of copper that had been coated with carbon during the evaporation phase and left to evaporate in the open air. The resolution of the TEM was 20 nm, and the length was 1.2 mm. It was operated between 40 and 100 keV. An ultrathin windowed liquid-nitrogen-cooled EDX was used to analyze the chemical makeup of the *VN*–$Fe_3O_4$–CuO nanocatalyst. XRD, (Ultima IV) was used to analyze the *VN*–$Fe_3O_4$–CuO nanocatalyst. After the nanocatalyst had been dried in a vacuum oven at 40 °C, the powder was manually grind. The *VN*–$Fe_3O_4$–CuO nanocatalyst exhibited a series of characteristic peaks at 34.05, 34.07, 36.11, 37.24, 40.04, 43.38, and 47.282.

**2.4.1. Synthesis of (3-(4-chlorophenyl)-4-methyl-6-phenyl pyrazolo[3,4-*c*]pyrazol-2(1*H*,3*H*,6*H*)-yl)(pyridin-4-yl)methanone 1a.** The *VN*–$Fe_3O_4$–CuO nanocatalyst (30 mol%) was added to a mixture containing 3-methyl-1-phenyl-1*H*-pyrazol-5(4*H*)-one (0.01 mol), benzaldehyde (0.01 mol), and isonicotinohydrazide (0.01 mol) in ethanol (10 mL) and the reaction mixture was refluxed for 30 min. The progress of the reaction was monitored using thin-layer chromatography. After completion of the reaction, the catalyst was filtered by hot water washing, and the filtered solution was extracted with ethyl acetate (10 mL × 3) and washed with saturated sodium bicarbonate (50 mL) and brine (30 mL). The organic layer was dried over anhydrous $Na_2SO_4$ and concentrated under reduced pressure to obtain the crude residue, which was purified by column chromatography on silica gel using hexane/EtOAc (4 : 6, v/v) to produce the desired product. The above method was followed to synthesize other compounds (**1b–1l**). Physical constants, spectral data, molecular mass, and analytical values of compounds (**1a–1l**) are provided in the ESI files.†

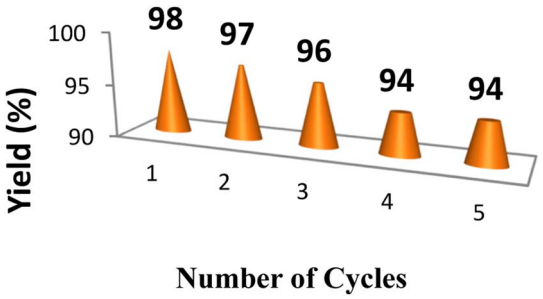


Fig. 6 Recycling of the *VN*–$Fe_3O_4$–CuO nanocatalyst for the synthesis of compound **1a**.

Open Access Article. Published on 02 de gener 2024. Downloaded on 16/2/2026 20:04:58.
This article is licensed under a Creative Commons Attribution-NonCommercial 3.0 Unported Licence.

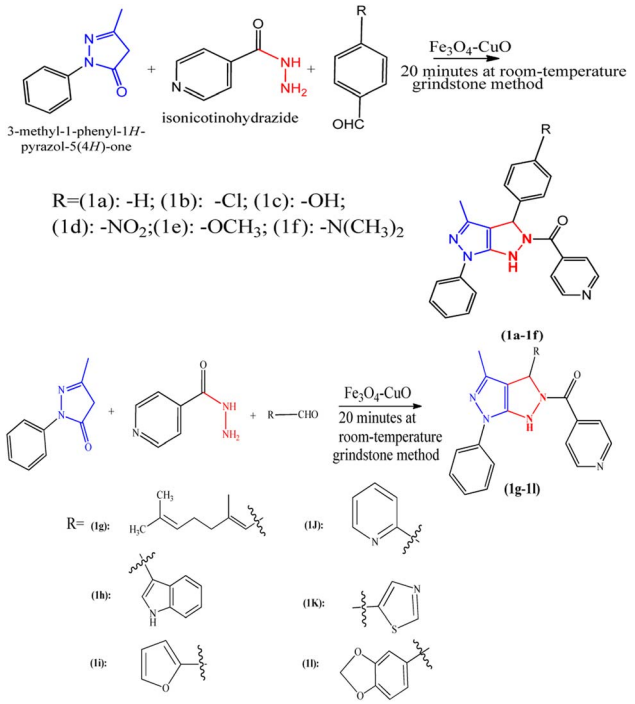


Scheme 2 The synthetic route of pyrazolo[3,4-*c*]pyrazole derivatives.

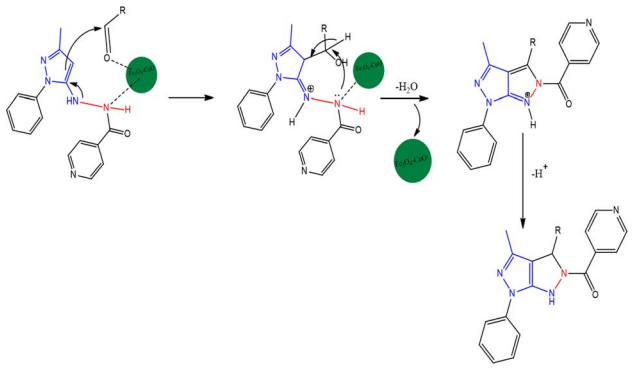


Scheme 3 The possible mechanism for the synthesis of pyrazolo[3,4-*c*]pyrazole derivatives.

### 2.5. Recyclability study

The stability and catalytic activity of the *VN*–$Fe_3O_4$–CuO nanocatalyst synthesized using the green method was assessed through a recycling experiment. Using a conventional approach, the reaction was performed as previously described. Following the reaction, the catalyst was filtered, washed with hot water, and dried for 3 h at 80 °C in a vacuum oven before the next cycle, as shown in (Fig. 6).

### 2.6. Biological activity

The antimicrobial activity of the concentrated extracts was tested on nine bacterial strains, including both Gram-positive and Gram-negative strains, which were obtained from the Microbial Type Culture Collection (MTCC) located at the Institute of Microbial Technology in Chandigarh, India. (See ESI† for full details).

**2.6.1. Antibacterial activity.** The disk diffusion method was used to evaluate the activity of each compound.[29] Gram-positive bacteria were *Enterococcus Faecalis* (MTCC 439), *Staphylococcus aureus* (MTCC 96), and other bacteria whereas Gram-negative bacteria examined were *Pseudomonas aeruginosa* (MTCC 739), *Klebsiella pneumonia* (MTCC 109), and *Escherichia coli* (MTCC 739). DMSO was used to dissolve each test sample at a concentration of 100 μg $mL^{-1}$. Inhibition was determined following a 24-hour incubation period at 37 °C. Ciprofloxacin was used as the test compound.

**2.6.2. Antifungal activity.** All compounds were subjected to agar dilution testing to assess their antifungal activity.[29] The compounds (**1a–1l**), *Candida albicans* (MTCC 183), *Microsporum audouinii* (MTCC 739), *Cryptococcus neoformans* (a clinical isolate), and *Aspergillus niger* (MTCC 872), were used in this study. DMSO (100 μg $mL^{-1}$) was used to determine the sample concentration. Clotrimazole was the standard for comparison of the test compounds.

**2.6.3. Minimum inhibitory concentration (MIC) studies.** To determine the minimal inhibitory concentrations (MICs) of compounds (**1a–l**), their 64 μg $mL^{-1}$ solutions were subjected to successive two-fold dilutions, furnishing samples with concentrations of 64, 32,…, and 0.25 μg $mL^{-1}$. Microbial suspensions of 106 CFU $mL^{-1}$ (CFU = colony forming unit) were inoculated in the corresponding wells, and the plates were incubated at 36 °C for 24 h. The MICs were determined as the lowest concentrations completely inhibiting the visible growth of microorganisms.

**2.6.4. Cell lines and cell cultures.** The American-type cell collection produced MCF-7 cell lines; the cell lines and cell culture details are available in the ESI.†

**2.6.5. Cytotoxic activity.** The cytotoxicity of the synthesized compounds (**1a–1l**) was assessed following the experimental procedure discussed previously.[30,31]

### 2.7. Molecular docking

**2.7.1. Preparation of ligands.** ChemDraw 12.0 was used to draw the ligand molecules (**1a–1l**), and Chem3Dpro's MM2 force field was used to minimise the energy.

**2.7.2. Preparation of receptor.** The ternary complex of *Escherichia coli* and *Candida albicans* and proteins' 3D of the Protein Data bank's proteins' 3D crystal structures were downloaded using PDB IDs 1AI9 and 1AJ0. Discovery Studio 2019 was used to remove water molecules and ligands from the receptor. The SWISS PDB Viewer software was utilized to minimize the energy consumption of the receptor during the molecular docking analysis.

**2.7.3. Identification of binding pocket.** Discovery Studio 2019 was used for the identification of the binding pockets of the target protein that contains Phe 36, Asn 22, Thr 62, Arg 63, Arg 255, Arg 63, Arg 255, and Ile 257 residues.

**2.7.4. Docking.** The interactions of the binding modes between compounds (**1a–1l**), 1AI9, and IAJ0 proteins were examined using the Auto Dock Vina 1.1.2 program for


© 2024 The Author(s). Published by the Royal Society of Chemistry

Open Access Article. Published on 02 de gener 2024. Downloaded on 16/2/2026 20:04:58.
This article is licensed under a Creative Commons Attribution-NonCommercial 3.0 Unported Licence.

Table 1 Optimization study of the reaction conditions for **1a**

| S. no. | Catalysis | Reaction condition, RM, grindstone method | Mol percentage of catalysis | Yield |
|---|---|---|---|---|
| 1 | CuO | 1 min | 10 | — |
| | | | 20 | — |
| | | | 30 | — |
| | | 10 min | 10 | — |
| | | | 20 | — |
| | | | 30 | — |
| | | 20 min | 10 | — |
| | | | 20 | — |
| | | | 30 | 10 |
| | | 30 min | 10 | — |
| | | | 20 | — |
| | | | 30 | 23 |
| 2 | $Cu(OAc)_2$ | 1 min | 10 | — |
| | | | 20 | — |
| | | | 30 | — |
| | | 10 min | 10 | — |
| | | | 20 | 12 |
| | | | 30 | 14 |
| | | 20 min | 10 | — |
| | | | 20 | 15 |
| | | | 30 | 17 |
| | | 30 min | 10 | — |
| | | | 20 | 13 |
| | | | 30 | 26 |
| 3 | $Fe_2O_3$ | 1 min | 10 | — |
| | | | 20 | — |
| | | | 30 | — |
| | | 10 min | 10 | — |
| | | | 20 | — |
| | | | 30 | 12 |
| | | 20 min | 10 | — |
| | | | 20 | 12 |
| | | | 30 | 24 |
| | | 30 min | 10 | — |
| | | | 20 | 15 |
| | | | 30 | 32 |
| 4 | $Fe_3O_4$ | 1 min | 10 | — |
| | | | 20 | — |
| | | | 30 | — |
| | | 10 min | 10 | — |
| | | | 20 | — |
| | | | 30 | 14 |
| | | 20 min | 10 | — |
| | | | 20 | — |
| | | | 30 | 12 |
| | | 30 min | 10 | — |
| | | | 20 | — |
| | | | 30 | 17 |
| 5 | *VN*–$Fe_3O_4$–CuO | 1 min | 10 | — |
| | | | 20 | 10 |
| | | | 30 | 15 |
| | | 10 min | 10 | 37 |
| | | | 20 | 48 |
| | | | 30 | 82 |
| | | 20 min | 10 | 63 |
| | | | 20 | 81 |
| | | | 30 | 94 |
| | | 30 min | 10 | 89 |
| | | | 20 | 92 |
| | | | 30 | 98 |

Open Access Article. Published on 02 de gener 2024. Downloaded on 16/2/2026 20:04:58. This article is licensed under a Creative Commons Attribution-NonCommercial 3.0 Unported Licence.

Table 2 The minimal inhibitory concentrations of the compounds (1a–1l)[a]

| | Antibacterial activity | | | | | | | | |
|---|---|---|---|---|---|---|---|---|---|
| | Gram-negative bacteria | | | Gram-positive bacteria | | Antifungal activity | | | |
| Com. no. | *E. c* | *P. a* | *K. p* | *S. a* | *E. f* | *A. n* | *C. a* | *C. n* | *M. a* |
| **1a** | 64 | 64 | 32 | >100 | >100 | 64 | 64 | >100 | >100 |
| **1b** | >100 | >100 | 4 | >100 | 8 | 8 | 0.25 | 32 | >100 |
| **1c** | 16 | 32 | >100 | >100 | 16 | >100 | 64 | >100 | 64 |
| **1d** | 32 | 64 | >100 | 64 | >100 | >100 | >100 | 64 | 32 |
| **1e** | 32 | >100 | >100 | 64 | 32 | 64 | 16 | >100 | 1 |
| **1f** | >100 | 16 | 8 | 8 | >100 | >100 | 32 | >100 | >100 |
| **1g** | 1 | 32 | 64 | >100 | 64 | 32 | 32 | 64 | 64 |
| **1h** | >100 | 32 | >100 | >100 | >100 | 64 | 32 | 4 | 0.5 |
| **1i** | 64 | >100 | 16 | 64 | 16 | >100 | >100 | 2 | 64 |
| **1g** | >100 | >100 | 32 | >100 | 32 | 16 | 64 | 16 | >100 |
| **1k** | 64 | >100 | 32 | 32 | >100 | 32 | >100 | 64 | >100 |
| **1l** | >100 | >100 | >100 | >100 | >100 | >100 | >100 | 64 | 64 |
| DMSO | – | – | – | – | – | – | – | – | – |
| (a)[b] | 32 | 64 | 32 | 0.12 | 16 | – | – | – | – |
| (b)[b] | – | – | – | – | – | 1 | 0.5 | 4 | 2 |

[a] The minus (–) represents inactive for screening. [b] Standard (a): ciprofloxacin; standard (b): clotrimazole.

molecular docking. The active amino acid residues in the binding pocket formed a docking grid box. The Pymol and Discovery Studio 2019 programming were used to visually analyse the interactions with the exhaustiveness value set to 8.[32–34]

**2.7.5. Molecular dynamics simulation.** Molecular dynamics simulation was conducted on the docked complexes identified through IFD analysis, utilising Desmond of Schrödinger Biosuite, to evaluate their stability.[35]

# 3. Results and discussion

## 3.1. Characterization of the *VN*–$Fe_3O_4$–CuO nanocatalyst

Identification of *Vitex Negundo* leaf extracts. Characteristic peaks for the hydroxyl compounds O–H (stretch) were obtained in the aqueous solution (3276 $cm^{-1}$). N–H (stretch), and C–N (stretch) characteristic peaks, in the aqueous extract at 1169 $cm^{-1}$ and 761 $cm^{-1}$.[36] The synthesized $Fe_2O_3$ exhibited a large broad band at 3396 $cm^{-1}$, which is ascribed to the O–H stretching vibration in the O–H groups. The peak at 1482 $cm^{-1}$ is attributed to the symmetric bending vibration of C=O.[37] The bands of the *VN*–$Fe_3O_4$–CuO nanocatalyst were observed at 3400 and 1271 $cm^{-1}$. The presence of the O–H stretching vibration was indicated by the band at 3400 $cm^{-1}$ in the *Vitex Negundo* leaf extract.[38] Peaks at 752 and 591 $cm^{-1}$ were utilized to demonstrate the development of CuO nanostructures as reducing and capping agents for the synthesis of the *VN*–$Fe_3O_4$–CuO nanocatalyst[39] (Fig. 2).

The *VN*–$Fe_3O_4$–CuO nanocatalyst was studied using UV-vis spectroscopy. The reaction mixture of the leaf extract and $Fe_3O_4$ solution immediately turned black because of the formation of the *VN*–$Fe_3O_4$–CuO nanocatalyst. Plant extracts contain bioactive molecules with hydroxyl groups that reduce iron to ferric hydroxide, which is partially converted into the *VN*–$Fe_3O_4$–CuO nanocatalyst by other bioactive compounds. In the visible region, the *VN*–$Fe_3O_4$–CuO nanocatalyst exhibited significant absorption at 242 nm, $Fe_2O_3$ absorption peak at 387 nm, and $Cu(OAc)_2$ absorption peak at 290, and the *VN*–$Fe_3O_4$–CuO nanocatalyst absorption peak changed slightly towards 230 nm, indicating that the *VN*–$Fe_3O_4$–CuO nanocatalyst 275 nm was formed (Fig. 3).

The solutions of the *VN*–$Fe_3O_4$–CuO nanocatalyst were spread over a carbon-coated grid at room temperature for TEM measurements. Fig. 4a and b show TEM images of the *VN*–$Fe_3O_4$–CuO nanocatalyst that were mostly spherical and 20–50 nm in size. The particle size distribution histogram was

Table 3 Cytotoxic activity of compounds (1a–1l)

| | $LC_{50}$[a] (μg $mL^{-1}$) | | |
|---|---|---|---|
| Compounds | MCF-7 cell line | Vero | SI[b] |
| **1a** | 78.10 ± 0.02 | 55.02 ± 0.11 | 0.70 |
| **1b** | 22.10 ± 0.04 | 65.23 ± 0.05 | 2.95 |
| **1c** | 70.10 ± 0.05 | 73.81 ± 0.07 | 1.05 |
| **1d** | 91.10 ± 0.06 | 83.36 ± 0.03 | 0.91 |
| **1e** | 23.62 ± 0.02 | 79.39 ± 0.09 | 3.36 |
| **1f** | 19.92 ± 0.01 | 82.10 ± 0.07 | 4.12 |
| **1g** | 30.82 ± 0.04 | 65.66 ± 0.06 | 4.11 |
| **1h** | 21.43 ± 0.03 | 88.10 ± 0.05 | 2.75 |
| **1i** | 26.66 ± 0.05 | 73.45 ± 0.01 | 3.55 |
| **1j** | 57.34 ± 0.08 | 83.20 ± 0.02 | 1.45 |
| **1k** | 62.34 ± 0.07 | 78.01 ± 0.05 | 1.25 |
| **1l** | 69.12 ± 0.11 | 88.50 ± 0.02 | 1.28 |
| Doxorubicin | 0.65 ± 0.01 | 21.05 ± 0.82 | 32.38 |

[a] The mean values of three separate experiments are represented as mean ± standard error. [b] Selectivity index = $LC_{50}$ value normal cell/$LC_{50}$ value cancer cell.


© 2024 The Author(s). Published by the Royal Society of Chemistry

Open Access Article. Published on 02 de gener 2024. Downloaded on 16/2/2026 20:04:58.
This article is licensed under a Creative Commons Attribution-NonCommercial 3.0 Unported Licence.

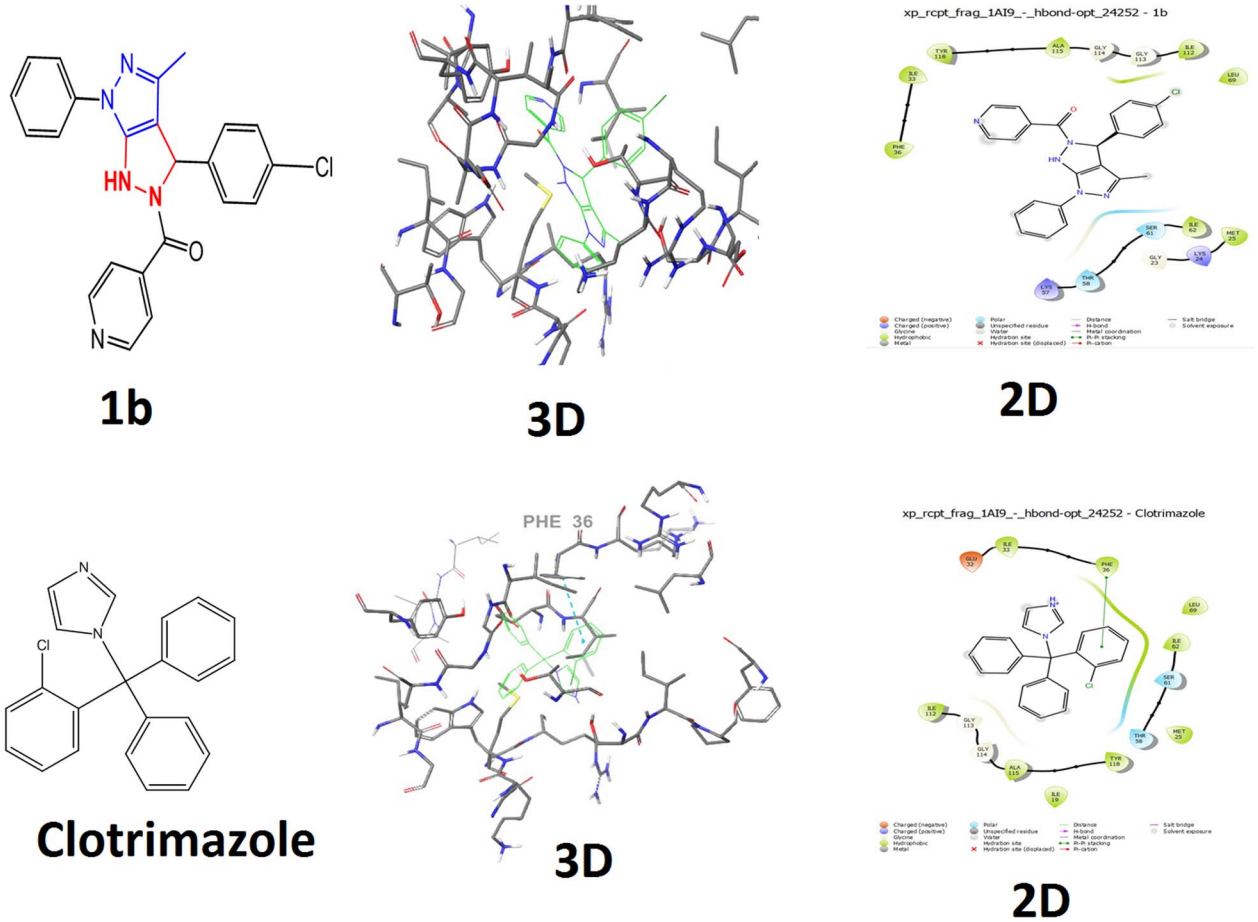


Fig. 7 Molecular docking studies for protein IAI9 (*Candida albicans*) docked with compound **1b** and clotrimazole with their 2D and 3D docking structures.

determined based on the sizes of 82 particles from the TEM image. The majority of the spherical nanocatalyst were single crystals. A characteristic optical absorption peak was observed at 0.5 keV, and EDAX detected Fe and oxygen, indicating the formation of the *VN*–$Fe_3O_4$–CuO nanocatalyst, as shown in Fig. 4c. The XRD patterns of the *VN*–$Fe_3O_4$–CuO nanocatalyst matched the (110), (311), (111), (400), (020), (422), and (311) Bragg reflections corresponding to the characteristic peaks at 34.05, 34.07, 36.11, 37.24, 40.04, 43.38, and 47.28, respectively. The $Cu(OAc)_2$ patterns matched the (110), (111), (311), (400), and (422) Bragg reflections corresponding to the characteristic peaks at 27.00, 31.14, 38.21, 44.06, 47.17, 51.24, 56.31, 59.28, 63.34, 65.07, and 67.032, respectively.

Each of these patterns matched the (110), (−111), (111), (−202), (020), (−113), (−311), (220), (311), and (222) Bragg reflections corresponding to the characteristic XRD peaks as 24.06, 28.12, 31.46, 34.72, 51.04, 54.16, 57.31, 65.28, and 56.28 2 for $Fe_2O_3$. These patterns were matched to the (012), (104), (110), (113), (024), (116), (0.16), (214), and (300) Bragg reflections according to the JCPDS standard magnetite XRD patterns (JCPDS card no. 19-0629) (Fig. 5). The wide-angle XRD peaks of *VN*–$Fe_3O_4$–CuO nanocatalyst were easily identified as those of pure cubic phase. Since the impurity peaks were absent, *VN*–$Fe_3O_4$–CuO nanocatalyst of high purity was prepared successfully.

### 3.2. Catalytic activity and characterization of pyrazolo[3,4-*c*] pyrazole derivatives

The synthetic route of pyrazolo[3,4-*c*]pyrazole derivatives is shown in Scheme 2, and the possible mechanism is shown in Scheme 3. The catalyst optimization processes for the synthesis of **1a** are shown in Table 1. The reaction was carried out for 1 min with 10 mol of catalysts, and no yield was obtained. However, when the *VN*–$Fe_3O_4$–CuO catalyst was used for 1 min with 20 mol of the catalyst a 10% yield, and 30 mol of catalyst gave a 15% yield. CuO, $Cu(OAc)_2$, $Fe_2O_3$, and $Fe_3O_4$ showed no significant yields at 10 min with 10–30 mol, whereas *VN*–$Fe_3O_4$–CuO showed 37, 48, and 82% yields corresponding to 10, 20, and 30 mol in the reaction, respectively. At a reaction time of 20 min, the catalytic performance was not significant even at all concentrations, whereas the *VN*–$Fe_3O_4$–CuO catalyst gave yields of 63, 81, and 94% in the presence of 10, 20, and 30 mol of catalyst, respectively. The CuO catalyst in 30 min with 30 mol showed 23% yield; the catalyst $Cu(OAc)_2$ in 30 min with 30 mol showed 26% yield only; the catalyst $Fe_2O_3$ in 30 min with 30 mol showed only 32% yield. The highest yield was obtained when

Open Access Article. Published on 02 de gener 2024. Downloaded on 16/2/2026 20:04:58.
This article is licensed under a Creative Commons Attribution-NonCommercial 3.0 Unported Licence.

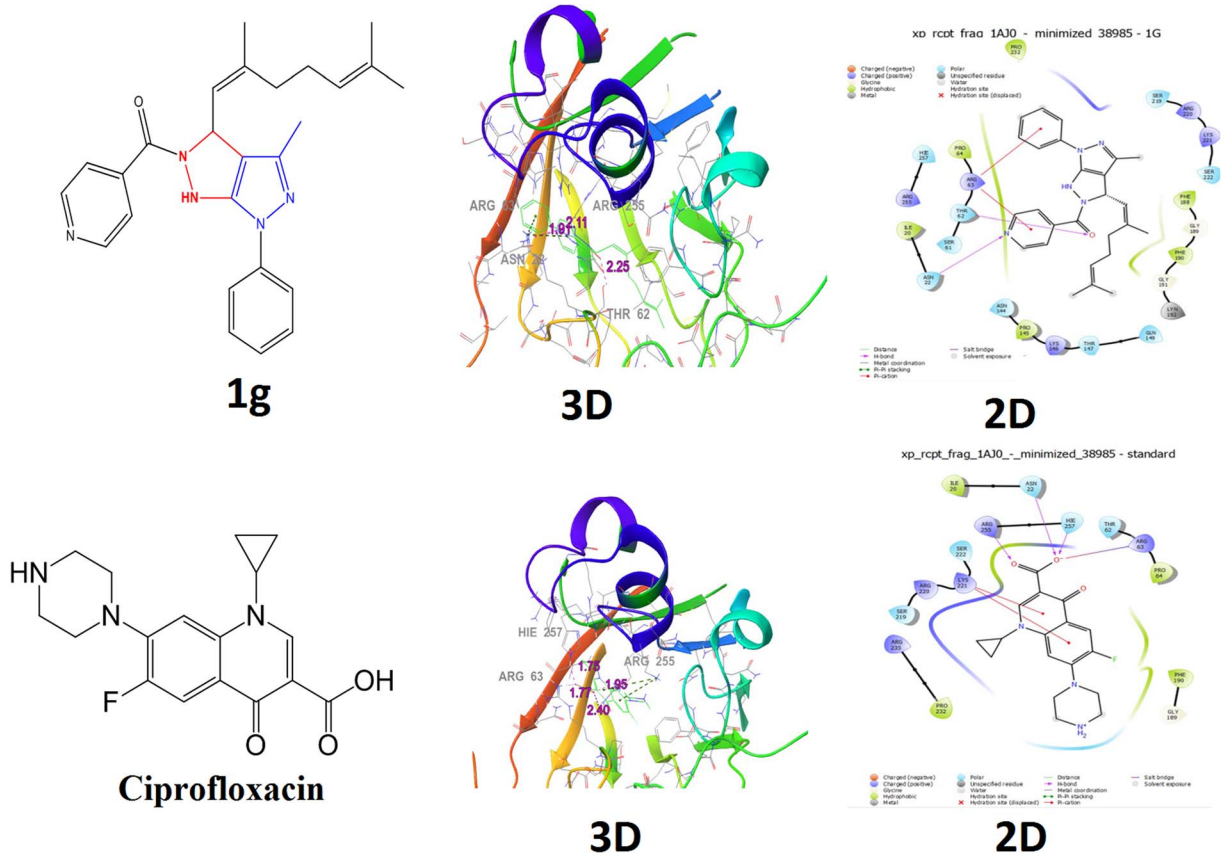


Fig. 8 Molecular docking studies for protein 1AJ0 (*Escherichia coli*) docked with compound **1g** and ciprofloxacin with their 2D and 3D docking structures.

the *VN*–$Fe_3O_4$–CuO catalyst was used with 30 mol, at 30 min it gave a 98% yield. The final product of compound **1a** was confirmed by spectroscopic characterization. The IR absorption bands showed that compound **1a** frequency ranged between 3323, 2974, 1655, and 1640 $cm^{-1}$, corresponding to the –NH, –C=O, and –C=N groups, respectively. For compound **1a**, $^1$H NMR spectral value showed a sharp singlet at $\delta$ 1.97 for $CH_3$ proton, $\delta$ 8.36 (d, $J$ = 6.23 Hz), 7.83 (d, $J$ = 6.22 Hz), 7.62–7.45 (t, $J$ = 6.21 Hz), 7.30–7.17, 6.13, and 4.0 ppm corresponding to the –Ar ring, –CH, and –NH. $^{13}$C NMR spectra of compound peaks at $\delta$ 172.0, 149.0–105.7, 149.7–121.7, 142.8–123.9, 68.1, and 12.7 ppm corresponding to C=O, pyridine, Ar ring, –CH, and –$CH_3$ carbons, respectively. The $^1$H and $^{13}$C NMR spectra of (**1a–1l**) are included in the ESI file (Fig. S1–S24†).

Table 2 shows the results of testing of all the compounds against various fungal species for antifungal activity. Compound **1b** showed high activity against *Candida albicans* (MIC: 0.25 μg $mL^{-1}$) than clotrimazole (MIC: 0.5 μg $mL^{-1}$). Compound **1h** was effective against *Microsporum audouinii* (MIC: 0.5 μg $mL^{-1}$), whereas **1i** (MIC: 2 μg $mL^{-1}$) was more active than *Cryptococcus neoformans* with a standard clotrimazole (MIC: 4 μg $mL^{-1}$). DMSO was inactive in all fungal and bacterial species.

### 3.3. Cytotoxic activity

The cytotoxic activity of the synthesized compounds (**1a–1l**) was evaluated against the MCF-7 cell line and normal Vero cell line, and all of them showed low activity compared to other standard

Table 4 Molecular docking results for compounds **1b** and **1g**

| Compound name | Dock score | Interacting residues | Bond length |
|---|---|---|---|
| **Protein 1AI9 (*Candida albicans*) binds with ligand** | | | |
| **1b** | −4.8 | — | — |
| Clotrimazole | −4.4 | Phe36 | 5.38 |
| **Protein IAJ0 (*Escherichia coli*) binds with ligand** | | | |
| **1g** | −3.7 | Asn22, Thr62, Arg63, Arg255 | 1.91, 2.25, 3.24, 2.11 |
| Ciprofloxacin | −5.6 | Arg63, Arg255(2), Ile257 | 1.77, 1.95, 2.40, 1.75 |


© 2024 The Author(s). Published by the Royal Society of Chemistry

Open Access Article. Published on 02 de gener 2024. Downloaded on 16/2/2026 20:04:58.
This article is licensed under a Creative Commons Attribution-NonCommercial 3.0 Unported Licence.

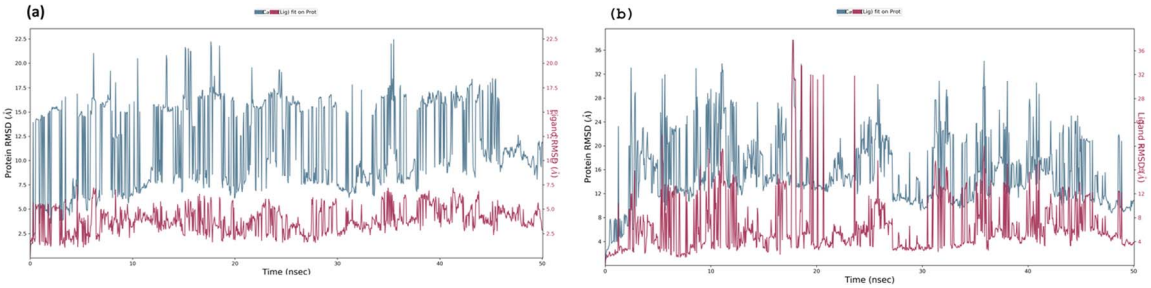


Fig. 9 (a) RMSD plot of 1AI9 docked with **1b**. (b) RMSD plot of 1AJ0 docked with **1g**.

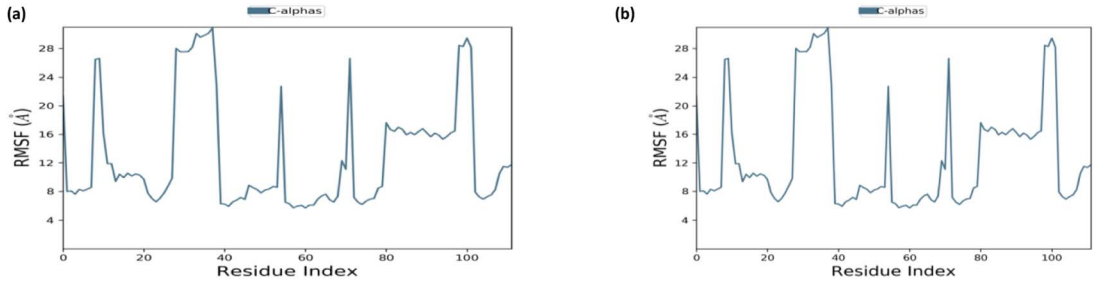


Fig. 10 (a) RMSF plot of 1AI9 docked with **1b**. (b) RMSF plot of 1AJ0 docked with **1g**.

doxorubicin ($LC_{50}$: 21.05 ± 0.82 μg $mL^{-1}$), as shown in Table 3 (see ESI† for full details). The chosen Vero cell line was based on previously reported literature.[40,41]

### 3.4. Docking results

*In silico* antibacterial and antifungal activity results of the selected ligands against dihydrofolate reductase (DHFR enzyme) from *Candida albicans* (PDB ID: 1AI9)[42] and *Escherichia coli* were inhibited by docking the synthesized compounds; protein (PDB ID: 1AJ0) was evaluated using the AutoDock Vina program. Dihydrofolate reductase (PDB ID: 1AI9)[43] are reported in terms of binding energy and ligand interactions in order to predict the binding energy of ligands within the binding site of the target proteins, as shown in (Fig. 7 and 8).

The docking score of compound **1b** (−4.8 kcal $mol^{-1}$) and no bond length compared with those of standard clotrimazole (−4.4 kcal $mol^{-1}$) docking score and bond length (5.38). Compound **1b** showed no interacting residues and clotrimazole, as shown in (Fig. 7). The *Candida albicans* binding protein (PDB ID: 1AI9) and the positive control clotrimazole are shown in (Fig. 7). The hydrophobic interactions: GLY 23, LYS 24, MET 25, ILE 33, PHE 36, LYS 57, THR 58, SER 61, ILE 62, LEU 69, ILE 112, GLY 113, GLY 114, ALA 115, and TYR 118. According to the results, clotrimazole, the control, and compound **1b** exhibited equivalent levels of inhibition, as shown in Table 4. The positive control clotrimazole was connected to the *Candida albicans* binding protein (PDB ID: 1AI9) and amino acids ILE 19, MET 25, GLU 32, ILE 33, PHE 36, TH 58, SER 61, ILEV62, LEU 69, ILE 112, GLY 113, GLY 114, and ALA 115, as shown in (Fig. 7). The results showed that compound **1b** possessed inhibition abilities comparable with those of the control ciprofloxacin Table 4.

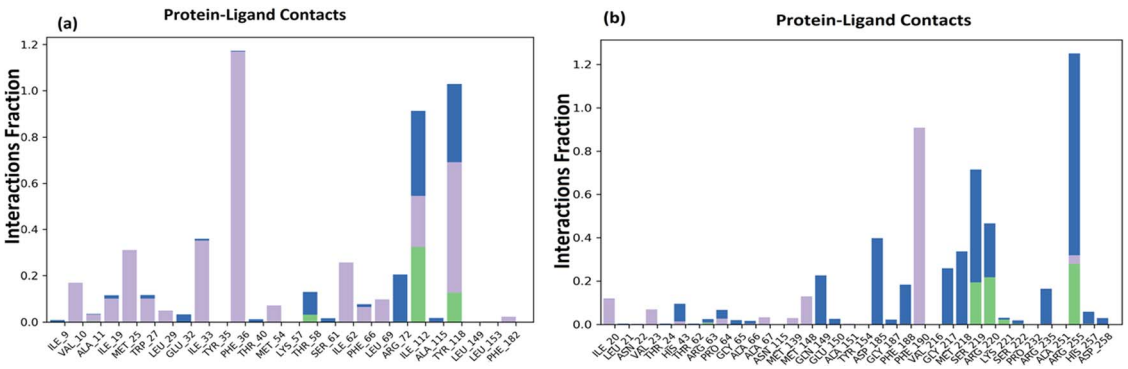


Fig. 11 (a) Histogram of protein–ligand contacts of 1AI9 docked with **1b**. (b) Histogram of protein–ligand contacts of 1AJ0 docked with **1g**.

Open Access Article. Published on 02 de gener 2024. Downloaded on 16/2/2026 20:04:58.
This article is licensed under a Creative Commons Attribution-NonCommercial 3.0 Unported Licence.

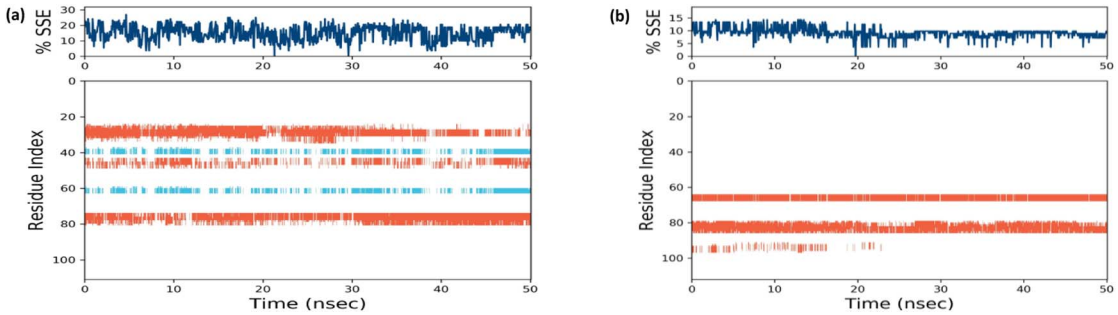


Fig. 12 (a) Timeline representation of protein–ligand contacts of 1AI9 docked with **1b**. (b) Timeline representation of protein–ligand contacts of 1AJ0 docked with **1g**.

Compound **1g** had a lower docking score (−3.7 kcal $mol^{-1}$), and its bond length is (3.24, 2.25, 2.11, and 1.91), interacting residues (ASN 22, THR 62, ARG 63 and ARG 255). The compound **1g** was connected to the crystal structure of a ternary complex of the *Escherichia coli* binding protein (PDB ID: 1AJ0) and hydrophobic interactions ILE 20, ASN 22, SER 61, THR 62, ARG 63, PRO 64, ASN 144, PRO 145, LYS 146, THRR 147, PHE 188, GLY 189, PHE 190, GLY 191, LYN 192, SER 219, ARG 220, LYS 221, SER 222, ARG 255, and HIE 257 (Fig. 8). Compound **1g** possessed inhibition abilities comparable to those of the control ciprofloxacin with docking score (−5.6 kcal $mol^{-1}$), bond length (2.40, 1.95, 1.77, and 1.75), and interacting residues (ARG 63, ARG 255(2), and ILE 257) shown in Table 4.

The standard ciprofloxacin was connected to the crystal structure of a ternary complex of the *Escherichia coli* binding protein (PDB ID: 1AJ0) and hydrophobic interactions ILE 20, ASN 22, THR 62, ARG 63, PRO 64, GLY 189, PHE 190, SER 219, ARG 220, LYS 221, SER 222, PRO 232, ARG 235, and HIE 257, as shown in (Fig. 8).

The control clotrimazole was involved in hydrophobic interactions with (PHE 36) and **1g** (ASN 22, THR 62, ARG 63, and ARG 255) of ciprofloxacin (ARG63, THR62, ARG 225(2), and ILE 257), which are the active site residues and they have multiple functions, including catalysis and substrate binding, as well as stabilising the intermediates and the structure of the binding cleft.

### 3.5. Molecular dynamics simulation

Docked complex structures of ligands **1b** and **1g** with proteins 1AI9 and 1AJ0 were studied using the molecular dynamics simulation by Desmond, Schrödinger to analyze the simulation and stability of the complexes, as shown in Fig. 9–12 (see ESI† for full details).

## 4. Conclusion

The synthesized *VN*–$Fe_3O_4$–CuO nanocatalyst showed high catalytic activity, and the *VN*–$Fe_3O_4$–CuO nanocatalyst was used to synthesize pyrazolo[3,4-*c*]pyrazole derivatives. The *VN*–$Fe_3O_4$–CuO nanocatalyst was investigated using FTIR, UV, TEM, and XRD. Compound **1g** (MIC: 1 μg $mL^{-1}$) was highly active against *Escherichia coli* compared with ciprofloxacin. For antimicrobial activity, compound **1b** (MIC: 0.25 μg $mL^{-1}$) demonstrated a higher antifungal activity against *Candida albicans* than clotrimazole, while compound **1g** (MIC: 1 μg $mL^{-1}$) showed a more powerful effect against *Escherichia coli* than ciprofloxacin. Compounds (**1a–1l**) showed significantly low cytotoxicity compared to the standard doxorubicin ($LC_{50}$: 21.05 ± 0.82 μg $mL^{-1}$). AutoDock Vina was used to consider compounds **1g** and **1b** along with the standards ciprofloxacin and clotrimazole with 1AJO and 1AI9 proteins. When compared with clotrimazole (−4.4 kcal $mol^{-1}$), the molecule **1b** showed a docking score (−4.8 kcal $mol^{-1}$), and the novel molecule **1g** displayed a respectable docking score (−3.7 kcal $mol^{-1}$) compared with the ciprofloxacin docking score (−5.6 kcal $mol^{-1}$) in the 1AJ0 protein. Furthermore, *in silico* analysis indicated that compounds **1b** and **1g** exhibited high docking scores. The results showed that test compounds had outstanding inhibitory abilities in antibacterial and antifungal properties compared to the standards. Therefore, these new pyrazolo[3,4-*c*]pyrazole derivatives could potentially be utilised as lead compounds in the development of novel and clinically useful classes of antimicrobial agents.

## Author contributions

J. M.; methodology, A. A.; molecular docking studies, H. M. A.; software analysis, I. A.; investigation and compound characterization. The manuscript was read and approved by all authors prior to publication.

## Conflicts of interest

There are no conflicts to declare.

## Acknowledgements

We extend our appreciation to the Researchers Supporting Project (RSPD2023R1083), King Saud University, Riyadh, Saudi Arabia.

## References

1 M. C. Ortiz and J. Portilla, Access to five-membered N-heteroaromatic compounds: Current approach based on

 © 2024 The Author(s). Published by the Royal Society of Chemistry

Open Access Article. Published on 02 de gener 2024. Downloaded on 16/2/2026 20:04:58.
This article is licensed under a Creative Commons Attribution-NonCommercial 3.0 Unported Licence.

microwave-assisted synthesis, *Targets Heterocycl. Syst.*, 2021, **25**, 436–462.
2 X. Jiang, K. Wu, R. Bai, P. Zhang and Y. Zhang, Functionalized quinoxalinones as privileged structures with broad-ranging pharmacological activities, *Eur. J. Med. Chem.*, 2022, **229**, 114085.
3 C. Sharma, Synthesis of some novel ethoxyphthalimide derivatives of pyrazolo[3,4-c]pyrazoles, *Indian J. Chem., Sect. B: Org. Chem. Incl. Med. Chem.*, 2008, **47**, 1892–1897.
4 T. Jiang, G. Wang, Y. Liu, L. Feng, M. Wang, J. Liu, Y. Chen and L. Ouyang, Development of small-molecule tropomyosin receptor kinase (TRK) inhibitors for NTRK fusion cancers, *Acta Pharm. Sin. B*, 2021, **11**, 355–372.
5 S. S. Kadam, L. Maier, I. Kostakis, N. Pouli, J. Toušek, M. Nečas, P. Marakos and R. Marek, Synthesis and Tautomerism of Substituted Pyrazolo [4, 3-c] pyrazoles, *Eur. J. Org Chem.*, 2013, **30**, 6811–6822.
6 S. Asadi, F. Alizadeh-Bami and H. Mehrabi, One-pot synthesis of functionalized pyrazolo [3, 4-c] pyrazoles by reaction of 2-cyano-N-methyl-acrylamide, aryl aldehyde, and hydrazine hydrate, *Arkivoc*, 2020, **part vi**, 238–246.
7 A. Saeed, A. M. Soliman, K. M. Al-Taisan, E. Abdel-Latif, A. A. Ahmed, Z. M. Alaizeri and H. A. Alhadlaq, Synthesis and molecular docking of new indeno [1, 2-d] imidazole, indeno [1, 2-e] triazine, indeno [1, 2-c] pyrazole, and indeno [1, 2-b] pyrrole polycyclic compounds as antibacterial and antioxidant agents, *J. Mol. Struct.*, 2023, **1289**, 135763.
8 Y. M. Youssef, M. E. Azab, G. A. Elsayed, A. A. El-Sayed, A. I. Hassaballah, M. M. El-Safty, R. A. Soliman and E. A. El-Helw, Synthesis and antioxidant, antimicrobial, and antiviral activity of some pyrazole-based heterocycles using a 2 (3 H)-furanone derivative, *J. Iran. Chem. Soc.*, 2023, **3**, 1–4.
9 K. A. acobson, S. Merighi, K. Varani, P. A. Borea, S. Baraldi, M. Aghazadeh Tabrizi, R. Romagnoli, P. G. Baraldi, A. A. Ciancetta, D. K. Tosh and Z. G. Gao, A3 adenosine receptors as modulators of inflammation: from medicinal chemistry to therapy, *Med. Res. Rev.*, 2018, **38**, 1031–1072.
10 D. A. Berry, L. L. Wotring, J. C. Drach and L. B. Townsend, Synthesis and Biological Activity of the Novel Adenosine Analogs; 3-Amino-6-(β-D-ribofuranosyl) pyrazolo [3, 4-c] pyrazole and 3-Amino-1-methyl-6-(β-D-ribofuranosyl) pyrazolo [3, 4-c] pyrazole, *Nucleosides, Nucleotides Nucleic Acids*, 1994, **13**, 405–420.
11 D. Raffa, B. Maggio, M. V. Raimondi, S. Cascioferro, F. Plescia, G. Cancemi and G. Daidone, Recent advanced in bioactive systems containing pyrazole fused with a five membered heterocycle, *Eur. J. Med. Chem.*, 2015, **97**, 732–746.
12 N. M. Saleh, M. G. El-Gazzar, H. M. Aly and R. A. Othman, Novel anticancer fused pyrazole derivatives as EGFR and VEGFR-2 dual TK inhibitors, *Front. Chem.*, 2020, **7**, 917.
13 S. M. Gomha, H. M. Abdel-aziz and A. A. El-Reedy, Facile Synthesis of Pyrazolo [3, 4-c] pyrazoles Bearing Coumarine Ring as Anticancer Agents, *J. Heterocycl. Chem.*, 2018, **55**, 1960–1965.
14 F. Turkan, A. Cetin, P. Taslimi, M. Karaman and I. Gulçin, Synthesis, biological evaluation and molecular docking of novel pyrazole derivatives as potent carbonic anhydrase and acetylcholinesterase inhibitors, *Bioorg. Chem.*, 2019, **86**, 420–427.
15 R. S. Kumar, I. A. Arif, A. Ahamed and A. Idhayadhulla, Anti-inflammatory and antimicrobial activities of novel pyrazole analogues, *Saudi J. Biol. Sci.*, 2016, **23**, 614–620.
16 P. B. Chouke, T. Shrirame, A. K. Potbhare, A. Mondal, A. R. Chaudhary, S. Mondal, S. R. Thakare, E. Nepovimova, M. Valis, K. Kuca and R. Sharma, Bioinspired metal/metal oxide nanoparticles: A road map to potential applications, *Mater. Today Adv.*, 2022, **16**, 100314.
17 A. Almatroudi, Silver nanoparticles: Synthesis, characterisation and biomedical applications, *Open Life Sci.*, 2020, **15**, 819–839.
18 A. B. Afzal, M. J. Akhtar, M. Nadeem and M. M. Hassan, Investigation of structural and electrical properties of polyaniline/gold nanocomposites, *J. Phys. Chem.*, 2009, **113**, 17560–17565.
19 J. Xiong, Y. Wang, Q. Xue and X. Wu, Synthesis of highly stable dispersions of nanosized copper particles using L-ascorbic acid, *Green Chem.*, 2011, **13**, 900–904.
20 M. Aksoy, H. Kilic, B. Nişancı and O. Metin, Recent advances in the development of palladium nanocatalysts for sustainable organic transformations, *Inorg. Chem. Front.*, 2021, **8**, 499–545.
21 A. M. Eid, A. Fouda, S. E. D. Hassan, M. F. Hamza, N. K. Alharbi, A. Elkelish, A. Alharthi and W. M. Salem, Plant-Based Copper Oxide Nanoparticles; Biosynthesis, Characterization, Antibacterial Activity, Tanning Wastewater Treatment, and Heavy Metals Sorption, *Catalysts*, 2023, **13**, 348.
22 A. Ahmad, M. Khan, S. Khan, R. Luque, T. M. Almutairi and A. M. Karami, Bio-construction of MgO nanoparticles using Texas sage plant extract for catalytical degradation of methylene blue via photocatalysis, *Int. J. Environ. Sci.*, 2023, **20**, 1451–1462.
23 M. Hamk, F. A. Akçay and A. Avcı, Green synthesis of zinc oxide nanoparticles using Bacillus subtilis ZBP4 and their antibacterial potential against foodborne pathogens, *Prep. Biochem. Biotechnol.*, 2023, **53**, 255–264.
24 M. E. Czaikowski, A. J. McNeece, J. N. Boyn, K. A. Jesse, S. W. Anferov, A. S. Filatov and J. S. Anderson, Generation and Aerobic Oxidative Catalysis of a Cu (II) Superoxo Complex Supported by a Redox-Active Ligand, *J. Am. Chem. Soc.*, 2022, **144**, 15569–15580.
25 N. Das, D. Sarkar, M. M. Saikh, P. Biswas, S. Das, N. A. Hoque and P. P. Ray, Piezoelectric activity assessment of size-dependent naturally acquired mud volcano clay nanoparticles assisted highly pressure sensitive nanogenerator for green mechanical energy harvesting and body motion sensing, *Nano Energy*, 2022, **102**, 107628.
26 M. M. Shanwaz and P. Shyam, Synthesis of silver nanoparticles from Vitex negundo plant by green method and their bactericidal effects, *Lett. Appl. NanoBiosci.*, 2022, **12**, 59–62.

Open Access Article. Published on 02 de gener 2024. Downloaded on 16/2/2026 20:04:58.
This article is licensed under a Creative Commons Attribution-NonCommercial 3.0 Unported Licence.

27 J. Sichaem, H. H. Nguyen, V. H. Nguyen, D. H. Mac, D. T. Mai, H. C. Nguyen, T. N. M. Tran, N. K. T. Pham, H. H. Nguyen, N. Niamnont and T. H. Duong, A new labdane-type diterpenoid from the leaves of Vitex negundo L, *Nat. Prod. Res.*, 2021, **35**, 2329–2334.

28 M. Patel, J. Patel and R. Dayaramani, Green-nanotechnology-driven drug delivery systems. *Sustainable Nanotechnology: Strategies, Products, and Applications*, 2022, pp. 117–133.

29 R. S. Kumar, M. Moydeen, S. S. Al-Deyab, A. Manilal and A. Idhayadhulla, Synthesis of new morpholine-connected pyrazolidine derivatives and their antimicrobial, antioxidant, and cytotoxic activities, *Bioorg. Med. Chem.*, 2017, **27**, 66–71.

30 A. Idhayadhulla, A. Manilal, A. Ahamed, S. Alarifi and G. Raman, Potato Peels Mediated Synthesis of Cu (II)-nanoparticles from Tyrosinase Reacted with bis-(N-aminoethylethanolamine)(Tyr-Cu (II)-AEEA NPs) and Their Cytotoxicity against Michigan Cancer Foundation-7 Breast Cancer Cell Line, *Mol*, 2021, **26**, 6665.

31 L. Velmurugan, A. Ahamed, A. Idhayadhulla, S. Alarifi and R. Gurusamy, Antioxidant, antibacterial, and cytotoxic activities of Cimemoxin derivatives and their molecular docking studies, *J. King Saud Univ., Sci.*, 2023, 103011.

32 S. Chidambaram, M. A. El-Sheikh, A. H. Alfarhan, S. Radhakrishnan and I. Akbar, Synthesis of novel coumarin analogues: Investigation of molecular docking interaction of SARS-CoV-2 proteins with natural and synthetic coumarin analogues and their pharmacokinetics studies, *Saudi J. Biol. Sci.*, 2021, **28**, 1100–1108.

33 J. Mullaivendhan, A. Ahamed, G. Raman, S. Radhakrishnan and I. Akber, Synthesis and antibacterial activity of pyrano [3, 2-g] chromene-4, 6-dione derivatives and their molecular docking and DFT calculation studies, *Results Chem.*, 2023, **6**, 101175.

34 S. Chidambaram, D. Ali, S. Alarifi, R. Gurusamy, S. Radhakrishnan and I. Akbar, Tyrosinase-mediated synthesis of larvicidal active 1, 5-diphenyl pent-4-en-1-one derivatives against Culex quinquefasciatus and investigation of their ichthyotoxicity, *Sci. Rep.*, 2021, **11**, 20730.

35 M. H. S. Abuthakir, V. Sharmila and M. Jeyam, Screening Balanites aegyptiaca for inhibitors against putative drug targets in Microsporum gypseum–Subtractive proteome, docking and simulation approach, *Infect., Genet. Evol.*, 2021, **90**, 104755.

36 S. Pawar and V. Kamble, Phytochemical screening, elemental and functional group analysis of Vitex negundo L. leaves, *Int. J. Pharm.*, 2017, **9**, 226–230.

37 M. Farahmandjou and F. Soflaee. *Low Temperature Synthesis of α-Fe2O3 Nano-Rods Using Simple Chemical Route*, 2014.

38 N. Y. Chowdhury, W. Islam and M. Khalequzzaman, Insecticidal activity of compounds from the leaves of Vitex negundo (Verbenaceae) against Tribolium castaneum (Coleoptera: Tenebrionidae), *Int. J. Trop. Insect Sci.*, 2011, **31**, 174–181.

39 G. Manjari, Green synthesis of silver and copper nanoparticles using Aglaia elaeagnoidea and its catalytic application on dye degradation, Doctoral dissertation, Department of Ecology and Environmental Sciences, Pondicherry University, 2018.

40 W. Zhang, S. Lun, S. S. Wang, Y. P. Cai, F. Yang, J. Tang and L. F. Yu, Structure-based optimization of coumestan derivatives as polyketide synthase 13- thioesterase (Pks13-TE) inhibitors with improved hERG profiles for Mycobacterium tuberculosis treatment, *ACS J. Med. Chem.*, 2022, **65**, 13240–13252.

41 O. O. Adeniji, M. O. Ojemaye and A. I. Okoh, Antibacterial Activity of Metallic Nanoparticles against Multidrug-Resistant Pathogens Isolated from Environmental Samples: Nanoparticles/Antibiotic Combination Therapy and Cytotoxicity Study, *ACS Appl. Bio Mater.*, 2022, **5**, 4814–4826.

42 A. H. Halawa, W. E. Elgammal, S. M. Hassan, A. H. Hassan, H. S. Nassar, H. Y. Ebrahim, A. B. Mehany and A. M. El-Agrody, Synthesis, anticancer evaluation and molecular docking studies of new heterocycles linked to sulfonamide moiety as novel human topoisomerase types I and II poisons, *Bioorg. Chem.*, 2020, **98**, 103725.

43 S. S. Madugula, S. Nagamani, E. Jamir, L. Priyadarsinee and G. N. Sastry, Drug repositioning for anti-tuberculosis drugs: an in silico polypharmacology approach, *Mol. Diversity*, 2022, **26**, 1675–1695.


© 2024 The Author(s). Published by the Royal Society of Chemistry